

1 Charged particle tracking without magnetic field:  
2 optimal measurement of track momentum by a Bayesian  
3 analysis of the multiple measurements of deflections due  
4 to multiple scattering

5 Mikael Frosini<sup>a</sup>, Denis Bernard<sup>a</sup>,

6 <sup>a</sup>*LLR, Ecole Polytechnique, CNRS/IN2P3, 91128 Palaiseau, France*

---

7 **Abstract**

8 We revisit the precision of the measurement of track parameters (position, angle)  
9 with optimal methods in the presence of detector resolution, multiple scattering  
10 and zero magnetic field. We then obtain an optimal estimator of the track  
11 momentum by a Bayesian analysis of the filtering innovations of a series of  
12 Kalman filters applied to the track.

This work could pave the way to the development of autonomous high-performance gas time-projection chambers (TPC) or silicon wafer  $\gamma$ -ray space telescopes and be a powerful guide in the optimisation of the design of the multi-kilo-ton liquid argon TPCs that are under development for neutrino studies.

13 *Key words:* track momentum measurement, multiple scattering, Kalman  
14 filter, Bayesian approach, noise covariance estimation, algebraic Riccati  
15 equation, magnetic-field free, time projection chamber, neutrino detector,  
16 gamma-ray telescope

---

17 **1. Introduction**

18 *1.1.  $\gamma$ -ray astronomy*

19 A huge effort is in progress to design  $\gamma$ -ray telescopes able to bridge the  
20 sensitivity gap that extends between the upper end of the high-sensitivity en-  
21 ergy range of past and present X-ray telescopes and the lower end of the high-

---

*Email addresses:* `denis.bernard` at `in2p3.fr` (Denis Bernard)

22 sensitivity energy range of the Fermi-LAT telescope, that is, approximately  
23  $0.1 - 100$  MeV.

24 On the low-energy side of the gap, tracking of the electron issued from the  
25 first Compton scattering of an incident photon enables a major improvement  
26 of the precision of the reconstruction of the direction of the incident photon  
27 ([1] and references therein) that induces an impressive improvement of the true-  
28 photon-background rejection and therefore of the point-like-source sensitivity.  
29 A serious limitation of that ETCC (electron tracking Compton camera) scheme  
30 arises though, as the effective area undergoes a sharp drop for photon energies  
31 above  $0.5$  MeV, due to the fact that the recoil electron can exit on the side and  
32 escape energy measurement [1]: electron momentum measurement inside the  
33 time projection chamber (TPC) itself is highly desirable.

34 On the high-energy side of the gap, novel approaches improve the sensitivity  
35 by improving the single-photon angular resolution by using converters having  
36 a lower- $Z$  than that of the tungsten plates of the EGRET / Fermi-LAT series.  
37 Using a series of silicon wafer active targets placed at a distance of each other,  
38 at the same time the material in which the photon converts and in which the  
39 tracks are tracked, enables an improvement of  $\approx$  a factor of three in the angular  
40 resolution at  $100$  MeV with respect to the LAT [2–9] at the cost of a lower aver-  
41 age active target density. Similar values of the angular resolution are achieved  
42 using a high-spatial-resolution, homogeneous, high-density material such as an  
43 emulsion [10].

44 If the trend to lower densities is pushed to the use of a gaseous detector,  
45 the angular resolution with respect to the LAT can increase up to a factor  
46 of ten at  $100$  MeV [11] and the single-track angular resolution is so good that  
47 the azimuthal angle of the  $e^+e^-$  pair can be measured with a good enough  
48 precision to enable the measurement of the linear polarization fraction of the  
49 incident radiation [12–14]. Gas detectors enable the detection of low-energy  
50 photons close to the pair-creation threshold where most of the statistics lie for  
51 cosmic sources (Fig. 1 of [15]), something which is critical for polarimetry.

52 Astrophysicists also need to measure the energy of incoming photons and

53 therefore the momentum of the conversion electron(s). This can be achieved  
54 using a number of techniques.

- 55 • In a calorimeter, the total energy of the photon is absorbed and measured.
- 56 • In a magnetic spectrometer, the trajectory of a particle with electric charge  
57  $q$  and momentum  $p$  in a magnetic field  $B$  is curved with a curvature radius  
58  $\rho = p/(qB)$ : from a measurement of  $\rho$ , one obtains a measurement of  $p$   
59 and in the end of the photon energy  $E$ .
- 60 • In a transition radiation detector (TRD), the energy of the radiation emit-  
61 ted in the forward direction by a charged particle at the interface between  
62 two media that have different refraction indices is proportional to the  
63 Lorentz factor  $\gamma$  of the particle, enabling a direct measurement. The low  
64 number of emitted photons per track per interface has lead to the devel-  
65 opment of multi-foil systems that suffer destructive interference at high  
66 energies. Appropriate configurations have showed saturation values larger  
67 than  $\gamma \approx 10^4$ , which implies that a measurement can be done up to a  
68 photon energy of  $\approx 10$  GeV [16].

69 The low-density active targets that have been considered above can provide  
70 a large effective area telescope only with a large volume ( $\mathcal{O}(\text{m}^3)$ ) and therefore  
71 the mass of the additional device used for energy measurement is a serious issue  
72 onboard a space mission. **In this document we first address the perfor-**  
73 **mance of the track momentum measurement from measurements of**  
74 **the angular deflections of charged tracks due to multiple scattering**  
75 **during the propagation in the tracker itself.**

## 76 *1.2. Large noble-liquid TPCs for neutrino physics*

77 Neutrino oscillation is a well established phenomenon and several experi-  
78 ments are being prepared with the goals:

- 79 • To test the occurrence of CP violation in the neutral lepton sector, i.e. to  
80 measure the only free complex phase  $\delta$  of the Pontecorvo-Maki-Nakagawa-

81 Sakata (PMNS) matrix with enough precision to determine its non-compatibility  
82 with zero,

- 83 • To determine unambiguously the 3 neutrino mass ordering, i.e. to solve  
84 the sign ambiguity of the square mass difference  $\Delta m_{31}^2$ .

85 Not only the (vacuum propagation) phase term that involves  $\delta$  changes sign  
86 upon  $\nu \leftrightarrow \bar{\nu}$  exchange, but the term that describes the interaction with matter  
87 changes sign too as our Earth contains much more electrons than positrons. “In  
88 the few-GeV energy range, the asymmetry from the matter effect increases with  
89 baseline as the neutrinos pass through more matter, therefore an experiment  
90 with a longer baseline [is] more sensitive to the neutrino mass hierarchy. For  
91 baselines longer than  $\approx 1200$  km, the degeneracy between the asymmetries from  
92 matter and CP-violation effects can be resolved” [17]. Large distances imply  
93 low fluxes, that is, huge detectors and, to match the  $\sin(\Delta m L/4E_\nu)$  oscillation  
94 function, high-energy neutrinos. So we should be prepared to measure the  
95 momentum of high-momentum muons in huge non-magnetised detectors such  
96 as liquid argon (lAr) TPCs.

97 The DUNE experiment expects to be able to measure muon momenta with  
98 a relative precision of  $\approx 18\%$  [18], based on a past ICARUS work [19]. They  
99 “anticipate that the resolution will deteriorate for higher-energy muons because  
100 they scatter less”, though. Given the  $dE/dx$  of  $0.2$  GeV/m of minimum ionising  
101 particles in lAr, a typical  $6$  GeV/ $c$  muon produces a long track: it should be  
102 interesting to study to what extent an optimal analysis of the thousands of  
103 measurements per track, at their  $\approx 3$  mm sampling pitch, can do better.

### 104 *1.3. Track momentum measurement from multiple scattering*

105 The measurement of track momentum using multiple scattering was pio-  
106 neered by Molière [20] and has been used since, in particular in the context of  
107 emulsion detectors (recent accounts can be found in [21, 22]).

108 In a practical detector consisting of  $N$  detection layers, the precision of  
109 the deflection measurement and therefore of the momentum measurement is

110 affected by the precision,  $\sigma$ , of the measurement of the position of the track  
111 when crossing each layer: the combined square deflection angle summed up over  
112 the whole track length therefore includes contributions from both the scattering  
113 angle and the detector precision. Bernard has optimized the longitudinal “cell”  
114 length over which each deflection angle is measured [11] and obtains a value of  
115 the relative momentum precision  $\sigma_p/p$  that scales as  $p^{1/3}$ , but the fact that the  
116 track position precision can improve when the cell length is extended and several  
117 measurements are combined was not taken into account in [11]. **In the present**  
118 **document we study an optimal method of momentum measurement**  
119 **with a tracker that has a finite (non zero) precision.**

120 In Section 2 we revisit optimal tracking methods in a context where the  
121 momentum of the particle is known. This allows us to present concepts and  
122 notations that are used later in the paper. We also extend the results published  
123 in the past by the use of more powerful methods.

124 The optimal precision of track measurements obtained in Sec. 2 can be ob-  
125 tained by performing the fit with a Kalman filter (KF), a tool that was imported  
126 in our field by Frühwirth [23]. In section 3 we give a brief summary of Kalman  
127 filter tracking in a Bayesian formalism. In magnetic spectrometers, the particle  
128 momentum takes part both in the particle state vector through the curvature of  
129 the trajectory and in the magnitude of multiple scattering. The precision of the  
130 magnetic measurement is most often so good that the momentum can rightfully  
131 be considered as being perfectly known in the expression of the multiple scat-  
132 tering. In our case of a zero magnetic field, it is not the case. A Kalman filter is  
133 the optimal estimate for linear system models with additive white noise, such is  
134 the case for multiple scattering (process noise) and detector precision (measure-  
135 ment noise), but at the condition that the optimal Kalman gain be used in the  
136 expression, that is, that the track momentum be known. In section 4, we use the  
137 Bayesian method developed by Matisko and Havlena [24] to obtain an optimal  
138 estimator of the process noise covariance, and therefore of the track momentum

139 <sup>1</sup>. We implement this method and characterize its performance on Monte Carlo  
 140 (MC) simulated tracks. We check that the momentum measurement is unbiased  
 141 within uncertainties. We obtain a heuristic analytical expression of the relative  
 142 momentum uncertainty.

143 Numerical examples are given for a homogeneous gas detector such as an  
 144 argon TPC and for a silicon-wafer detector:

- 145 • TPC gas, argon, 5 bar,  $\sigma = l = 0.1$  cm,  $L = 30$  cm [12];
- 146 • Silicon detector  $N = 56$ ,  $\Delta x = 500$   $\mu\text{m}$ -thick wafers spaced by  $l = 1$  cm,  
 147 with a single point precision of  $\sigma = 70$   $\mu\text{m}$  [8].

In this work a number of approximations are done: only the Gaussian core of the multiple-scattering angle distribution is considered and the non-Gaussian tails due to large-angle single scatters are neglected. The small logarithmic correction term in the expression of the RMS multiple scattering angle,  $\theta_0$ , is neglected

$$\theta_0 \approx \frac{p_0}{\beta p} \sqrt{\frac{\Delta x}{X_0}}, \quad (1)$$

148 where  $p_0 = 13.6$  MeV/ $c$  is the “multiple-scattering constant”,  $\Delta x$  is the matter  
 149 thickness through which the particle propagates and  $X_0$  is its radiation length  
 150 (Eqs. (33.14), (33.15), (33.17) of [26]). In the case of a homogeneous detector,  
 151 the thickness of the scatterer is equal to the length of the longitudinal sampling,  
 152  $l = \Delta x$ . We assume relativistic particles ( $\beta \approx 1$ ) without loss of generality.  
 153 Only the first-order term (angle deflection) of multiple scattering is taken into  
 154 account which is legitimate for the thin detectors considered here; the 2nd-order  
 155 transverse displacement (eq. (33.19) of [26]) is neglected. Continuous ( $dE/dx$ )  
 156 and discrete (BremsStrahlung radiation) energy losses are also neglected. In  
 157 TPCs in which the signal is sampled, most often the electronics applies a shaping

---

<sup>1</sup>Attempts of estimation of track momenta based on the use of a Kalman filter have been performed in the past, with little success. The un-validated un-characterized study of Ref. [25], for example, shows a poor relative resolution of  $\sigma_p/p = 30 - 40\%$  and that does not vary with the true particle momentum between 50 MeV/ $c$  and 2 GeV/ $c$ , which is a bad symptom.

158 of the pulse before digitisation, that creates a short scale longitudinal correlation  
 159 between successive measurements that we neglect too. Also the limitations of  
 160 pattern recognition, that is, in the case of  $\gamma$ -ray telescopes, of the assignment  
 161 of each hit to one of two close tracks, are not addressed.

162 Note that in the two main parts of this work (section 2 and sections 3-4)  
 163 we have made our best to follow the notations of Refs. [27, 28] and of [24],  
 164 respectively, and that they turn out to differ to some extent.

## 165 2. Tracking

An optimal tracking makes use of the full  $N \times N$  covariance matrix of the  $N$  measurements, including multiple scattering (correlation terms). This is most often impractical in modern trackers that provide a huge number of measurements for each track. The first successful attempt to perform a recursive determination of the covariance matrix was achieved by Billoir [27]. He considered the paraxial propagation of a charged track along the  $x$  axis inside a magnetic field oriented along  $z$ : close to the particle origin, the trajectory is a straight line in the  $(x, z)$  plane, and a parabola osculatrix to the true circle in the  $(x, y)$  plane. As we examine here the case of a magnetic-field-free tracker, the propagation (in the  $(x, z)$  and in the  $(x, y)$  planes) is approximated by straight lines (already using Innes notations [28] but assuming  $B = 0$ ):

$$y = a + b \times x. \tag{2}$$

166 Astronomers obviously have a special interest in the slope  $b$ , that is, in the  
 167 paraxial direction of the track at the conversion vertex.

The  $(a, b)$  correlation matrix is named  $V$  and the information matrix,  $I \equiv V^{-1}$ . Billoir develops a recursive method in which the fit propagates along the track, adding the information gain (measurement) and loss (scattering) at each layer. He obtains the information matrix at layer  $n + 1$  from the information matrix at layer  $n$  [27, 28]:

$$I_{n+1} = D^T (I_n^{-1} + B)^{-1} D + M, \tag{3}$$

where  $D$  is the drift matrix that propagates the track from layer  $n$  to layer  $n+1$ ,

$$D = \begin{bmatrix} 1 & l \\ 0 & 1 \end{bmatrix}, \quad (4)$$

$l$  is the layer spacing.  $B$  is the scattering matrix,

$$B = \begin{bmatrix} 0 & 0 \\ 0 & sl \end{bmatrix}, \quad (5)$$

where  $s \equiv \left(\frac{p_0}{p}\right)^2 \frac{\Delta x}{lX_0}$  is the average multiple-scattering angle variance per unit track length,  $\theta_0^2 = s \times l$ .  $M$  is the measurement matrix,

$$M = \begin{bmatrix} \iota l & 0 \\ 0 & 0 \end{bmatrix}, \quad (6)$$

168 where  $\iota \equiv \frac{N+5}{L\sigma^2} \approx \frac{1}{l\sigma^2}$  is the information density per unit track length,  $L =$   
 169  $N \times l$  is the full detector thickness.

170 Billoir considers the two particular cases of “scatters at one point” (detector  
 171 layers separated by an empty space) that we name here a segmented detector and  
 172 “uniformly distributed scattering” (homogeneous detector) [27]. These concepts  
 173 are defined more precisely below, following Innes [28].

#### 174 2.1. Segmented detector

Expressing  $I_n$  as  $I_n = A_n B_n^{-1}$  ([29], page 149) we obtain

$$\begin{bmatrix} A_{n+1} \\ B_{n+1} \end{bmatrix} = \begin{bmatrix} D^T + MD^{-1}B & MD^{-1} \\ D^{-1}B & D^{-1} \end{bmatrix} \begin{bmatrix} A_n \\ B_n \end{bmatrix}, \quad (7)$$

and

$$I_{n+1} = A_{n+1} B_{n+1}^{-1}. \quad (8)$$

Noting

$$\Phi \equiv \begin{bmatrix} D^T + MD^{-1}B & MD^{-1} \\ D^{-1}B & D^{-1} \end{bmatrix}, \quad (9)$$



we obtain

$$\begin{bmatrix} A_n \\ B_n \end{bmatrix} = \Phi^n \begin{bmatrix} A_0 \\ B_0 \end{bmatrix}. \quad (10)$$

$A_n$  and  $B_n$  are obtained from the eigenvalues of  $\Phi$ . The covariance matrix becomes  $V_n = B_n A_n^{-1}$ . We initialise the recurrence with  $A_0 = I_0 = 0$ ,  $B_0 = 1$ .

If  $\begin{bmatrix} A_n \\ B_n \end{bmatrix}$  is a solution of eq. (8), then for any  $\beta > 0$ ,

$$\frac{1}{\beta^n} \begin{bmatrix} A_n \\ B_n \end{bmatrix} = \frac{1}{\beta^n} \Phi^n \begin{bmatrix} A_0 \\ B_0 \end{bmatrix} \quad (11)$$

is a solution too. Noting  $\tilde{A}_n = \frac{A_n}{\beta^n}$ ,  $\tilde{B}_n = \frac{B_n}{\beta^n}$ ,  $\tilde{\Phi} = \frac{\Phi}{\beta}$ , we obtain

$$\begin{bmatrix} \tilde{A}_n \\ \tilde{B}_n \end{bmatrix} = \tilde{\Phi}^n \begin{bmatrix} \tilde{A}_0 \\ \tilde{B}_0 \end{bmatrix}, \quad (12)$$

with  $V_n = \tilde{B}_n \tilde{A}_n^{-1}$ .  $\Phi$  is found to satisfy

$$\Phi^T J \Phi = J, \quad (13)$$

with

$$J = \begin{bmatrix} 0 & 0 & 1 & 0 \\ 0 & 0 & 0 & 1 \\ -1 & 0 & 0 & 0 \\ 0 & -1 & 0 & 0 \end{bmatrix}, \quad (14)$$

from which  $\Phi$  is a symplectic matrix. General theorems enable a classification of  $\Phi$  eigenvalues into two ‘‘invert’’ and ‘‘conjugate’’ blocks, respectively (eq. (10) of [30])

$$\left\{ \alpha, \alpha^*, \frac{1}{\alpha}, \frac{1}{\alpha^*} \right\}, \quad (15)$$

where ‘‘\*’’ denotes complex conjugation. We choose  $\alpha$  to have a norm larger than unity,  $|\alpha| > 1$ . We obtain [31]

$$\alpha(x) = \frac{1}{2} j x^2 + \frac{1}{2} (-x^4 + 4j x^2)^{\frac{1}{2}} + 1, \quad (16)$$

where  $j$  is the imaginary unit and  $x \equiv \frac{l}{\lambda}$  is the detector longitudinal sampling normalized to the detector scattering length at momentum  $p$  [28]:

$$\lambda \equiv \frac{1}{\sqrt[4]{\iota s}}. \quad (17)$$

175 An exploration of the consequences of a variation of the initialisation of the  
 176 recurrence parameters shows that the system converges to the same solution  
 177  $\alpha(x)$  regardless of the values of  $A_0, B_0$ .  $B_0 \neq 0$  is needed so that  $I_0$  is defined.  
 178 With  $B_0 = 1, I_0 = A_0 = 0$  simply assumes that no *a priori* information is known  
 179 about the track.

We study the convergence of the covariance matrix while the Billoir mechanism is in progress along the track (increasing  $n$ ) by setting  $\beta = |\alpha|$ , that is,  $\tilde{\Phi} = \frac{1}{|\alpha|}\Phi$ .  $\tilde{\Phi}$  has two eigenvalues with modulus unity and two eigenvalues with modulus  $\frac{1}{|\alpha|^2}$ . The unity-modulus eigenvalues could be a major nuisance in the behaviour of  $I_n$  as a function of  $n$ , but when applying the Billoir mechanism we observe that for some reason the amplitude the so-induced oscillating terms is zero. The convergence behaviour is then driven by the two other eigenvalues, that is, by terms proportional to  $\frac{1}{|\alpha|^{2n}}$ . That exponential convergence is illustrated in Fig. 1 that shows the value of the detector thickness normalized to the detector scattering length,  $u$  [28],

$$u \equiv \frac{L}{\lambda}, \quad (18)$$

180 for which  $\frac{1}{|\alpha|^{2n}} < 10^{-4}$ , as a function of  $x$ .

181 Note that the homogeneousness parameter  $x$  and the thickness parameter  $u$   
 182 have a similar dependence on track momentum  $p$ , as  $u = x \times N$ .

### 183 2.1.1. Segmented detector: Thick detector limit

The asymptotic expression at high  $n$ , that is, at high  $u$  (thick detector) is reached after the Billoir mechanism (eq. (3)) has converged: we obtain the discrete Riccati equation:

$$I = D^T (I^{-1} + B)^{-1} D + M. \quad (19)$$

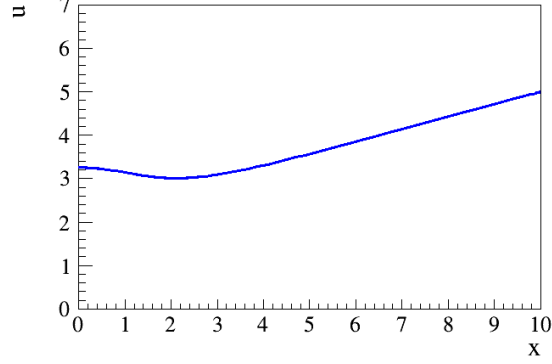


Figure 1: Value of  $u$  for which  $\frac{1}{|\alpha|^{2n}} < 10^{-4}$  as a function of  $x$  (from eq. (16)). For  $x < 5$ , convergence is reached for a detector thickness of  $4\lambda$ .

184 When the geometric, the multiple scattering and the measurement properties  
 185 of the detector are uniform (at least piecewise) the dynamics of the particle is  
 186 described by a time-invariant system and eq. (19) is referred to as the “algebraic”  
 187 Riccati equation (DARE). Equation (19) has four solutions, but the fact that  
 188 the asymptotically stable solution must be positive definite (Theorem 2.2 of  
 189 [30]) leaves us with only one.

190 *Segmented detector: Exact solution.*

We obtain [31]

$$V = \begin{pmatrix} \frac{4l^3 s}{x^3 (2x + \sqrt{x^2 + 4j} - \sqrt{x^2 - 4j})} & \frac{sl^2 (\sqrt{x^2 + 4j} + \sqrt{x^2 - 4j})}{x^2 (\sqrt{-x^2 - 4j} - \sqrt{4j - x^2} - 2jx)} \\ -\frac{4l^2 s}{x^2 (\sqrt{-x^2 - 4j} - jx) (jx + \sqrt{4j - x^2})} & \frac{2ls (\sqrt{x^2 + 4j} + \sqrt{x^2 - 4j})}{(x + \sqrt{x^2 + 4j}) (jx + \sqrt{4j - x^2})} \end{pmatrix}. \quad (20)$$

191 Even though it is not explicit from eq. (20),  $V$  is found to be a real matrix,  
 192 which is decent for a covariance matrix.

193 *Segmented thick detector: Small  $x$  behaviour: Homogeneous detector limit.*

The Taylor expansion close to  $x = 0$  is found to be

$$V_{aa} = \frac{\sqrt{2}}{i\lambda} \left[ 1 - \frac{x}{\sqrt{2}} + \frac{3}{8}x^2 - \frac{\sqrt{2}}{8}x^3 + \frac{9}{128}x^4 + O[x^5] \right], \quad (21)$$

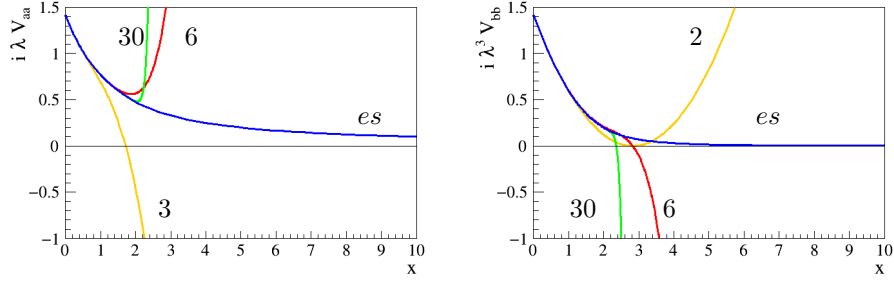


Figure 2: Thick detector:  $i\lambda V_{aa}$  and  $i\lambda^3 V_{bb}$  as a function of  $x$ . Comparison of the Taylor expansions to several orders, eqs. (21) and (22) to the exact solution “es”, eq. (20).

$$V_{bb} = \frac{\sqrt{2}}{i\lambda^3} \left[ 1 - \frac{x}{\sqrt{2}} + \frac{1}{8}x^2 + \frac{x^3}{128} - \frac{1}{1024}x^4 + O[x^5] \right]. \quad (22)$$

194 These expressions are similar<sup>2</sup> to what was found by Billoir ([27], p364, no  
 195 magnetic field) and Innes ([28], eq. (8), magnetic field). The Taylor expansion  
 196 is found to converge for  $x \lesssim 2$  (Fig. 2).

197 *Segmented thick detector: Large  $x$  behaviour: Coarse segmentation limit.*

198 The asymptotic behaviour of the coarsely instrumented detector (high  $x$ ) is presented in Fig. 3.

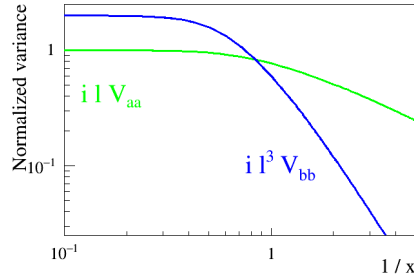


Figure 3: Thick detector: Normalized variance  $i\lambda V_{aa}$  and  $i\lambda^3 V_{bb}$  as a function of  $1/x$  (eq. (20)).

<sup>2</sup>We have detected a misprint, though: the factor  $-5/8$  in their expressions of  $V_{aa}$  is here corrected to  $3/8$ .

199

For  $1/x = 0$  we obtain  $ilV_{aa} = 1$  and  $il^3V_{bb} = 2$ , that is the obvious

$$V_{aa} = \sigma^2, \quad V_{bb} = 2 \left( \frac{\sigma}{l} \right)^2 : \quad (23)$$

200 the scattering is so intense that the intercept (angle) measurement is based on  
 201 the first (two first) layer(s), respectively. A thick coarse detector can be defined  
 202 by  $1/x < 0.5$ , that is,  $l > 2\lambda$  (Fig. 3). The  $\frac{1}{x}$  Taylor expansion is:

$$V_{aa} = \frac{1}{il} \left[ 1 - \frac{1}{x^4} + O\left(\frac{1}{x^8}\right) \right], \quad (24)$$

$$V_{bb} = \frac{1}{il^3} \left[ 2 - \frac{10}{x^4} + O\left(\frac{1}{x^8}\right) \right]. \quad (25)$$

### 203 2.2. Homogeneous Detector

204 A homogeneous detector is described having  $l$  tend to 0 while  $s$  and  $z$  are  
 205 kept constants. Fig. 4 shows that for all values of  $u$ , the intercept and angle  
 variances become very close to the homogeneous limit ( $x = 0$ ) for  $x \lesssim 0.2$ .

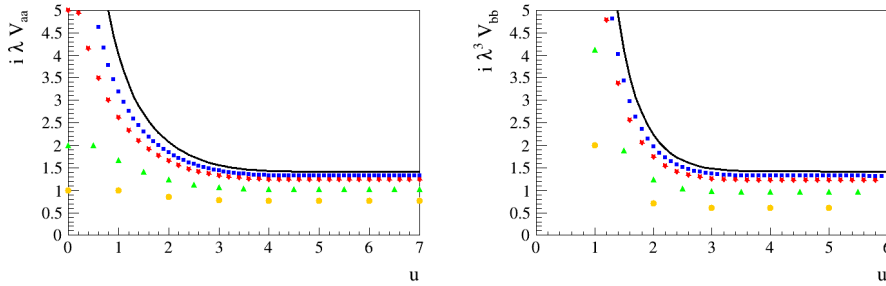


Figure 4: Normalized covariance coefficients  $ilV_{aa}$  (left) and  $il^3V_{bb}$  (right) as a function of  $u$  for various values of  $x \in \{0, 0.1, 0.2, 0.5, 1\}$ . Curve,  $x = 0$  (eq. (37)); squares,  $x = 0.1$ ; stars,  $x = 0.2$ ; triangles,  $x = 0.5$ ; bullets,  $x = 1.0$ . In both cases ( $a$  and  $b$ ),  $x \lesssim 0.2$  is found to be a good approximation of the homogeneous detector ( $x = 0$ ).

206

From the discrete evolution equation, eq. (3), and denoting  $I_n = I(nl) = I(L)$ , we obtain

$$\dot{I}(L) = D'^T I(L) + I(L)D' - I(L)B'I(L) + M', \quad (26)$$

where the dot denotes the derivation with respect to  $L$  and with

$$D' = \begin{bmatrix} 0 & 1 \\ 0 & 0 \end{bmatrix}, \quad B' = \begin{bmatrix} 0 & 0 \\ 0 & s \end{bmatrix}, \quad M' = \begin{bmatrix} i & 0 \\ 0 & 0 \end{bmatrix}. \quad (27)$$

After convergence (thick detector), we obtain the continuous algebraic Riccati equation (CARE):

$$D'^T I(L) + I(L) D' - I(L) B' I(L) + M' = 0, \quad (28)$$

207 *Homogeneous Detector: Small  $u$  behaviour.*

208 We first use Innes' method to compute an approximate solution. Attempting  
209 a Taylor expansion in  $u$ ,  $I(u) = \sum I^k u^k$ , we obtain:

$$\begin{aligned} I^0 &= 0, \\ I^1 &= M', \\ I^{k+1} &= \frac{1}{k+1} \left( - \sum_{i=0}^k I^i B' I^{k-i} + D'^T I^k + I^k D' \right). \end{aligned} \quad (29)$$

- In our case ( $B = 0$ , no curvature) we obtain:

$$V_{aa} = \frac{4}{i\lambda u} \left[ 1 + \frac{u^4}{416} - \frac{127u^8}{15\,891\,876\,000} + O(u^{12}) \right] \quad (30)$$

$$V_{bb} = \frac{12}{i\lambda^3 u^3} \left[ 1 + \frac{13u^4}{420} - \frac{13\,429u^8}{529\,200} + O(u^{12}) \right] \quad (31)$$

210

- For  $B \neq 0$  and a fit with curvature, we obtain the results of Innes (eq. (9) of [28]).

213 These Taylor expansions converge for  $u \lesssim 3.5$  (no curvature, Fig. 5) and  $u \lesssim 7.0$   
214 (with curvature, [28]). The thin detector ( $u = 0$ ) value of  $V_{bb}$  for  $B = 0$  is  
215 found to be smaller than that for  $B \neq 0$  by a factor of 16, as was discussed  
216 in the corrigendum of [11]: in a fit with curvature, the correlation between  
217 the curvature and the angle at the end(s) of the track degrades the angular  
218 resolution badly; this lasts until  $u \approx 1$  that is  $L \approx \lambda$  (plot not shown), after  
219 which all is flooded by multiple scattering anyway.

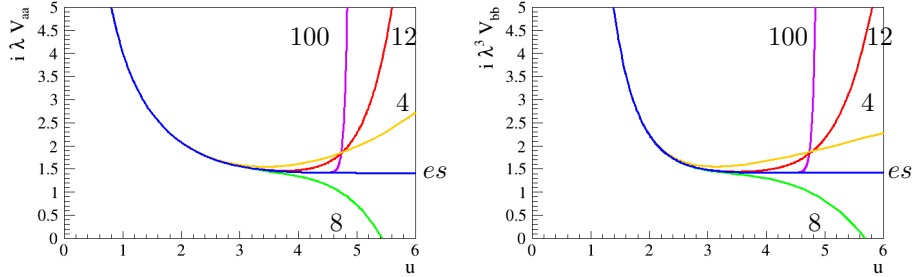


Figure 5: Homogeneous detector:  $i\lambda V_{aa}$  and  $i\lambda^3 V_{bb}$  as a function of  $u$ . Comparison of the Taylor expansions to several orders, eqs. (30) and (31), to the exact solution obtained from the resolution “es” of eqs. (33)-(34).

220 *Homogeneous Detector: Large  $u$  behaviour: Thick detector limit.*

Searching for expressions that are valid at high  $u$ , we follow again Innes and search a solution of the continuous equation for  $V$  that is similar to eq. (26) for  $I$ . Here the Taylor expansion is searched in  $1/u$ . Searching a solution parametrized as  $V(u) = V_0 + \frac{1}{u}V_1$ , we obtain

$$V_{aa} = \frac{\sqrt{2}}{i\lambda}, \quad V_{bb} = \frac{\sqrt{2}}{i\lambda^3}. \quad (32)$$

221 These values agree with that of eqs. (21), (22) for  $x = 0$ . The term proportional  
 222 to  $1/u$  that was present in the case with curvature (eq. (11) of [28]) cancels here,  
 223 which is related to the exponential convergence seen on eq. (37) (see also Fig.  
 224 7).

225 *2.2.1. Homogeneous thick detector: Exact solution*

We solve the continuous algebraic Riccati equation in a way similar to the discrete case [29]: Expressing

$$\Phi' = \begin{bmatrix} D' & M' \\ B' & -D'^T \end{bmatrix} \quad (33)$$

and  $I(L) = X(L)Y^{-1}(L)$ , and taking  $I(0) = 0$ , we obtain:

$$\begin{pmatrix} X(L) \\ Y(L) \end{pmatrix} = \exp[L\Phi'] \begin{pmatrix} 0 \\ 1 \end{pmatrix}. \quad (34)$$

$\Phi'$  satisfies

$$\Phi'^T J \Phi'^{-1} = -J \quad (35)$$

and is a hamiltonian matrix (section (4.8) of [29], [32]), which implies that  $\exp[\Phi']$  is a symplectic matrix and therefore that  $\Re\{\text{Tr}(\Phi')\} = 0$ . Furthermore all eigenvalues of  $\Phi'$  are found to be non singular [31]:

$$\text{Spec}(\Phi') = \left\{ \frac{1}{\lambda} e^{-\frac{3j\pi}{4}}, \frac{1}{\lambda} e^{-\frac{j\pi}{4}}, -\frac{1}{\lambda} e^{-\frac{3j\pi}{4}}, -\frac{1}{\lambda} e^{-\frac{j\pi}{4}} \right\}. \quad (36)$$

226 Solving eq. (34) we obtain [31]

$$V = \begin{pmatrix} \frac{\sqrt{2}}{\lambda^i} \frac{\left(-j + e^{2e^{\frac{j\pi}{4}}u} - e^{2e^{\frac{3j\pi}{4}}u} + je^{2j\sqrt{2}u}\right)}{\left(1 + e^{2e^{\frac{j\pi}{4}}u} + e^{2e^{\frac{3j\pi}{4}}u} - 4ej\sqrt{2}u + e^{2j\sqrt{2}u}\right)} & \frac{1}{\lambda^{2i}} \frac{\left(-1 + e^{2e^{\frac{j\pi}{4}}u}\right)\left(-1 + e^{2e^{\frac{3j\pi}{4}}u}\right)}{\left(1 + e^{2e^{\frac{j\pi}{4}}u} + e^{2e^{\frac{3j\pi}{4}}u} - 4ej\sqrt{2}u + e^{2j\sqrt{2}u}\right)} \\ \frac{1}{\lambda^{2i}} \frac{\left(-1 + e^{2e^{\frac{j\pi}{4}}u}\right)\left(-1 + e^{2e^{\frac{3j\pi}{4}}u}\right)}{\left(1 + e^{2e^{\frac{j\pi}{4}}u} + e^{2e^{\frac{3j\pi}{4}}u} - 4ej\sqrt{2}u + e^{2j\sqrt{2}u}\right)} & \frac{\sqrt{2}}{\lambda^{3i}} \frac{\left(j + e^{2e^{\frac{j\pi}{4}}u} - e^{2e^{\frac{3j\pi}{4}}u} - je^{2j\sqrt{2}u}\right)}{\left(1 + e^{2e^{\frac{j\pi}{4}}u} + e^{2e^{\frac{3j\pi}{4}}u} - 4ej\sqrt{2}u + e^{2j\sqrt{2}u}\right)} \end{pmatrix}. \quad (37)$$

227  
228 Even though it is not explicit from eq. (37),  $V$  is found to be a real matrix,  
229 which is decent for a covariance matrix. The convergence is driven by a term  
230 proportional to  $e^{-2ue^{\frac{j\pi}{4}}}$ , which implies a convergence in  $e^{-l\sqrt{2}/\lambda}$ .

### 231 2.2.2. Variation of the angle variance along the track

232 We have considered above the optimal measurement of the track parameters  
233 at the vertex,  $z = 0$ . Here we examine the measurement at any position along  
234 the track. A track now consists of two segments (left and right), the fit of each  
235 of which provides an estimate with its own covariance matrix.

236 A first combination attempt is performed on the two variables ( $a$  and  $b$ )  
237 separately. As is obvious, if the detector is thick on both sides, the two estimates  
238 (right, left) of a track parameter (say: the angle) have the same uncertainty on  
239 the plateau and their optimal combination provides a gain in RMS precision of  
240 a factor of  $\sqrt{2}$ . But that neglected the fact that in the combination, the other  
241 variable should be constrained to have the same value on both sides too. With  
242 a weighted variance estimation, a further gain of a factor of  $\sqrt{2}$  is obtained



243 on the plateau, that is a total gain of a factor of 2 with respect to individual  
 244 measurements (Fig. 6) as was observed experimentally by running a KF on  
 simulated tracks (Fig. 18 of [12]).

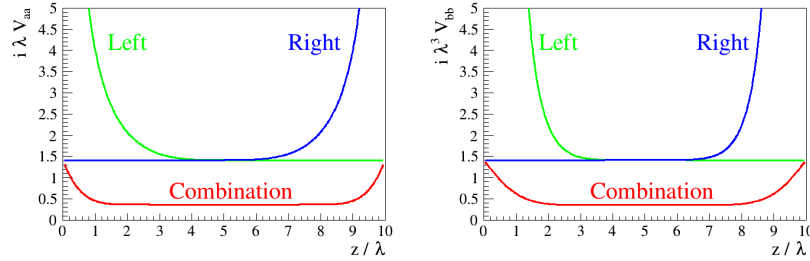


Figure 6: Normalized variance along the track for an  $u = 10$  detector, as estimated from the left and from the right side, (eq. (37)) and of their optimal combination. Left plot: intercept. Right plot: angle. An improvement of a factor of 4 is visible on the plateau (i.e., far from the track ends), that corresponds to a factor of 2 for the standard deviation.

245

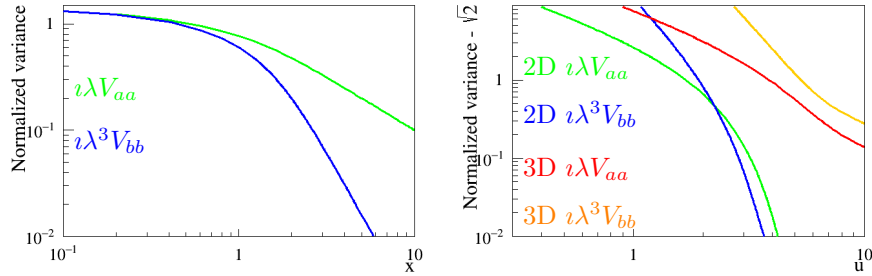


Figure 7: Exact solution wrap up: Thick detector (left) and homogeneous detector (right), for 2D ( $B = 0$ , no curvature) and 3D ( $B \neq 0$ , curvature) configurations. Normalized variance ( $i\lambda V_{aa}$ , and  $i\lambda^3 V_{bb}$ ) minus the asymptote (either zero or  $\sqrt{2}$ ), as a function of  $x$  and of  $u$ , respectively. Note that for the thick detector (left plots), the 2D and 3D expressions are found to be the same. Curves are from eq. (20) 2D thick detector and eq. (37) 2D homogeneous detector; the expressions in the 3D case are not shown in this paper.

246 *2.3. Optimal tracking: wrap up*

247 We now build on the results of the previous subsections to obtain expressions  
 248 of the variances in terms of the detector parameters. We do so for segmented

249 detectors. The expressions for continuous detectors can be obtained with  $\Delta x =$   
 250  $l$ .

251  $\iota \equiv \frac{1}{l\sigma^2}$  information density per unit track length

$s \equiv \left(\frac{p_0}{p}\right)^2 \frac{1}{X_0} \frac{\Delta x}{l}$  average multiple-scattering angle variance per unit track length

252  $\lambda \equiv \frac{1}{\sqrt[3]{\iota s}} \approx \sqrt{l\sigma \sqrt{\frac{X_0}{\Delta x}} \frac{p}{p_0}}$  detector scattering length at momentum  $p$

$x \equiv \frac{l}{\lambda} \approx \sqrt{\frac{l}{\sigma} \frac{p_0}{p} \sqrt{\frac{\Delta x}{X_0}}}$  detector longitudinal sampling normalized to  $\lambda$

$u \equiv \frac{L}{\lambda} \approx N \sqrt{\frac{l}{\sigma} \frac{p_0}{p} \sqrt{\frac{\Delta x}{X_0}}}$  detector thickness normalized to  $\lambda$

253 With:

254 • small  $x$  (large  $p$ ), homogeneous detector (continuous equation),

255 • large  $x$  (small  $p$ ), segmented detector (discrete equation)

256 and

257 • small  $u$  (large  $p$ ), thin detector,

258 • large  $u$  (small  $p$ ), thick detector.

259 The variances are found to be asymptotically:

		homogeneous $x < 0.2$		coarse $x > 2$
a	thin	$\frac{4}{i\lambda u} = \frac{4\sigma^2}{N}$	eq. (30)	
	thick 260	$\frac{\sqrt{2}}{i\lambda} = \sqrt{2} \left(\frac{p}{p_0}\right)^{-1/2} (l\sigma^3)^{1/2} \left(\frac{\Delta x}{X_0}\right)^{1/4}$	eq. (32)	$\frac{1}{il} = \sigma^2$ eq. (23)
b	thin	$\frac{12}{i\lambda^3 u^3} = \frac{12\sigma^2}{l^2 N^3}$	eq. (31)	
	thick 261	$\frac{\sqrt{2}}{i\lambda^3} = \sqrt{2} \left(\frac{\sigma}{l}\right)^{1/2} \left(\frac{\Delta x}{X_0}\right)^{3/4} \left(\frac{p}{p_0}\right)^{-3/2} = \left(\frac{p}{p_1}\right)^{-3/2}$	eq. (32)	$\frac{2}{u^3} = 2 \left(\frac{\sigma}{l}\right)^2$ eq. (23)

where  $p_1$  is a momentum that characterises the tracking angular-resolution properties of a detector affected by multiple scattering [12]

$$p_1 = p_0 \left(\frac{\Delta x}{X_0}\right)^{1/2} \left(\frac{2\sigma}{l}\right)^{1/3}. \quad (38)$$

- 262 • The two  $V_{aa}$  asymptotes cross for  $u = u_{c,a} = 2\sqrt{2} \approx 2.83$ ;
- 263 • The two  $V_{bb}$  asymptotes cross for  $u = u_{c,b} = (12/\sqrt{2})^{1/3} \approx 2.04$ .

This, for a given detector, takes place for a value of the momentum  $p_u$  for which

$$u_c = N \sqrt{\frac{l}{\sigma} \frac{p_0}{p} \sqrt{\frac{\Delta x}{X_0}}}, \quad (39)$$

that is,

$$p_u = p_0 \sqrt{\frac{\Delta x}{X_0} \frac{N^2 l}{\sigma u_c^2}}, \quad (40)$$

from which

$$u = u_c \sqrt{\frac{p_c}{p}}, \quad p = p_u \left(\frac{u_c}{u}\right)^2. \quad (41)$$

- 264 In short, a homogeneous detector is a thick detector,  $u > u_c$ , at low mo-  
265 mentum,  $p < p_u$  and a thin detector at higher momentum. In Table 1, we use  
266  $u_c = 2.5$  to compute the value of  $p_u$ .

Table 1: Parameters of two trackers considered in the text.

	gas argon TPC	liquid argon TPC	silicon detector		
$X_0$	2351.	14.0	9.4	cm	
$l$	0.1	0.3	1.0	cm	
$\Delta x$	$l$	$l$	0.0500	cm	
$\sigma$	0.1	0.1	0.0070	cm	
$L$	30.	1000.		cm	
$N$	300	3 333	56		
$p_1$	0.112	1.739	0.239	MeV/c	eq. (38)
$p_u$	1277.	10 614 042.	71 098.	MeV/c	eq. (40)
$p_x$	2.2	149.	3 542.	MeV/c	eq. (42)
$p_s$	0.024	5.4	16.6	MeV/c	eq. (61)
$p_\ell$	352.	2 931 742.	19 638.	MeV/c	eq. (62)

In the same way, a detector is a homogeneous detector,  $x < x_c$  at high momentum,  $p > p_x$ , with

$$p_x = p_0 \sqrt{\frac{\Delta x}{X_0}} \frac{l}{\sigma x_c^2}. \quad (42)$$

and  $x_c = 0.2$  (Fig. 4). And similarly:

$$x = x_c \sqrt{\frac{p_c}{p}}, \quad p = p_x \left(\frac{x_c}{x}\right)^2. \quad (43)$$

267 • **Argon gas TPC.** We see that  $p_u > p > p_x$  for most of the [1 MeV - 1 GeV]  
 268 momentum range that is the primary target of the high-performance  $\gamma$ -ray  
 269 telescopes mentioned above: the telescope is both a homogeneous and a  
 270 thick detector.

271 • **Silicon detector.** Here the telescope is a segmented and a thick detector  
 272 for most of the momentum range.

273 Note that the equality  $p_u = p_x$  holds for  $N = u_c/x_c$ , that is,  $N = 2.5/0.2 =$   
 274 12.5, so for most conceivable detectors,  $p_u > p_x$ , that is,

- 275 • if  $p > p_u$  then  $p > p_x$ , if a detector is thin for a given track, then it's also  
276 homogeneous;
- 277 • if  $p < p_x$  then  $p < p_u$ , if a detector is segmented for a given track, then  
278 it's also thick.

### 279 3. Kalman filter

280 A Kalman filter is an estimator of the state of a linear dynamic system per-  
281 turbed by Gaussian white noise using measurements that are linear functions  
282 of the system state and corrupted by additive Gaussian white noise [29]. The  
283 paraxial propagation of a high-momentum particle inside a detector is affected  
284 by angular deflections due to scattering on the charged particles (electrons,  
285 nuclei) present in the detector matter. Deflections undergone at different loca-  
286 tions on the track are uncorrelated, “white process noise”, and are approximated  
287 to have a Gaussian distribution under the multiple-scattering approximation.  
288 Transverse position measurements are performed at several locations along the  
289 track. They are affected by an uncertainty that does not correlate from layer  
290 to layer, “white measurement noise”, and that most often can be approximated  
291 by a Gaussian distribution. Angular deflections and measurement uncertainty  
292 are not correlated. When the system is non-linear, such as for the propaga-  
293 tion in a magnetic field, it is linearized locally, “extended Kalman filter” ([33]  
294 and references therein). In the case of most particle detectors, the geomet-  
295 ric, the multiple scattering and the measurement properties of the detector are  
296 uniform (at least piecewise) so the dynamics of the particle is described by a  
297 time-invariant system.

Since the founding work by Frühwirth [23], KF tracking has been used largely  
in high-energy physics. We present here a short description of the elements that  
are used in the next section, in a Bayesian formulation. Denoting  $\{z_n^0\}$  and  $\{z_n^m\}$   
the true and the measured positions of a particle at layer  $n$ , respectively, and  $x_n$   
the corresponding state vector,  $\hat{x}_n = \mathbb{E}(x_n | z_0^m, \dots, z_n^m)$  is the estimator of  $x_n$   
conditioned to  $\{z_0^m, \dots, z_n^m\}$  and  $x_n^{n-1} = \mathbb{E}(x_n | z_0^m, \dots, z_{n-1}^m)$  is the prediction

of  $x_n$  given  $\{z_0^m, \dots, z_{n-1}^m\}$ .  $x_n$  is obtained from  $x_{n-1}$

$$x_n = D \cdot x_{n-1} + D \cdot \begin{bmatrix} 0 \\ u_n \end{bmatrix}; \quad (44)$$

298  $u_n$  is the Gaussian-distributed deflection angle with variance  $sl$ . The covari-  
 299 ance matrix of the state vectors is  $P_n = \mathbb{E}((\hat{x}_n - x_n)(\hat{x}_n - x_n)^T | z_0, \dots, z_n^m)$ .  
 300 The optimal estimator of  $x_n$  is obtained from  $\hat{x}_{n-1}$  and from the measurements  
 301  $\{z_0^m, \dots, z_{n-1}^m\}$ ,

$$x_n^{n-1} = D\hat{x}_{n-1}, \quad (45)$$

$$P_n^{n-1} = D(P_{n-1} + B)D^T, \quad (46)$$

with

$$z_m^n = Hx_n + v_n, \quad (47)$$

302 where  $H = \begin{bmatrix} 0 & 1 \end{bmatrix}$  is the measurement matrix and  $v_n$  is the measurement un-  
 303 certainty which is Gaussian-distributed with variance  $\sigma^2 = \frac{1}{il}$ . The innovations  
 304 are the difference between measurement and prediction,

$$\nu_n = z_n^m - x_n^{n-1} \quad (48)$$

305 and their variance is

$$S_n = \text{Cov}(\nu_n) = \sigma^2 + HP_n^{n-1}H^T. \quad (49)$$

The gain matrix of the filter is

$$K_n = P_n^{n-1}H^T S_n^{-1}. \quad (50)$$

306 For the optimal value of the gain that minimizes the variance of the innova-  
 307 tions, we obtain [29]

$$\hat{x}_n = x_n^{n-1} + K_n \nu_n, \quad (51)$$

$$P_n = P_n^{n-1} - K_n S_n K_n^T. \quad (52)$$

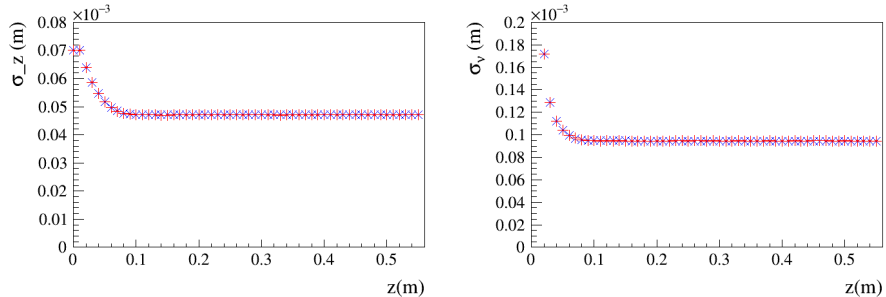


Figure 8: Kalman filter validation: RMS (plusses) of the position residues (left) and of the innovation residues (right) as a function of the longitudinal position in the tracker, for a sample of  $10^6$  50 MeV/c tracks in a silicon detector, compared to the RMS (crosses) computed from their variances,  $P_n$  and  $S_n$ , respectively.

308 Noting  $Z^n = z_0^m, \dots, z_n^m$  the set of measurements up to layer  $n$  and  $p$  the  
 309 probability density,

$$\begin{aligned}
 p(Z^n) &= p(z_n^m, Z^{n-1}) \\
 &= p(z_n^m | Z^{n-1}) p(Z^{n-1}) \quad (\text{Bayes}) \\
 &= \prod_{i=0}^n p(z_i^m | Z^{i-1}) \quad (\text{recurrence}). \quad (53)
 \end{aligned}$$

310 As  $z_i^m | Z^{i-1}$  is Gaussian distributed  $\mathcal{N}(z_i, S_i)$ :

$$p(z_i^m | Z^{i-1}) = \frac{1}{\sqrt{2\pi S_i}} \exp \left[ -\frac{\nu_i^2}{2S_i} \right]. \quad (54)$$

311 We have implemented such a KF tracking software. Figure 8 shows a couple  
 312 of sanity-check validation plots, the RMS of the position residues (left) and of  
 313 the innovation residues (right) as a function of the longitudinal position in the  
 314 tracker, for a sample of  $10^6$  50 MeV/c tracks in a silicon detector, compared to  
 315 the RMS computed from their variance,  $P_n$  and  $S_n$ , respectively.

#### 316 4. Momentum Measurement

317 A Kalman filter is the optimal linear estimator of the state vector of a dy-  
 318 namical system at the condition that the model be an accurate description of

319 the dynamics of the system and that the process and measurement noise covari-  
320 ance matrices be known, that is here, that the track momentum be known. The  
321 estimation of the noise covariance matrices of a dynamic system was pioneered  
322 by Mehra [34, 35] who studied and compared several methods:

- 323 • A Bayesian method that is the root of that we use in this work.
- 324 • Maximum likelihood methods, if necessary of both the state vector of the  
325 system and the noise matrices at the same time.

326 Bayesian and maximum likelihood methods were deemed to be too CPU con-  
327 suming for the time.

- 328 • Covariance-matching techniques, making the innovation residuals consis-  
329 tent with their theoretical covariances; these methods were shown later to  
330 give biased estimates of the covariance matrices.
- 331 • Correlation methods, in particular based on the observation that when the  
332 KF gain  $K$  is optimal, the innovations of the filtering process are white  
333 and Gaussian.

334 Mehra showed that the optimal gain  $K$  can be determined uniquely, after which  
335 many efforts and publications have then been spent in determining the conver-  
336 gence of these methods and to which values of the process and measurement  
337 noise matrices they were, eventually, converging. In 2006, Odelson *et al.* [36]  
338 re-examined Mehra's work, showed that the definite positiveness of the matrices  
339 was not assured; based on the fact that the autocorrelation of the innovation  
340 sequence is linearly dependent on the noise covariances [37], they developed an  
341 autocovariance least-square (ALS) method that provides unbiased estimates of  
342 the noise matrices and that includes a mechanism that enforces definite posi-  
343 tiveness [36].

344 Kalman filters have already been used for momentum measurement in non-  
345 magnetic particle physics detectors in the past ([38, 39]). The trick is to augment  
346 the state vector with the parameter vector to  $(x, y, dx/dz, dy/dz, 1/p)$  so that



347 the KF performs their estimation simultaneously. However, this augmentation  
 348 approach has been originally intended for estimating parameters in determin-  
 349 istic part of the model and its straightforward application for noise covariance  
 350 matrices does not result in appropriate estimates ([40] and references therein).

351 In the case of charged particle tracking in a magnetic-field-free detector, the  
 352 augmentation method was found to provide unbiased results though [38, 39],  
 353 most likely as the tracking part and the deflection part of the filter behave as  
 354 two separate filters, “only” linked by the joint uses of the track momentum, one  
 355 for the process noise matrix, the other as part of the state vector. Also it enables  
 356 the optimal treatment of energy loss and therefore it provides an improvement  
 357 of about a factor of two with respect to the Molière method [39]. It would be  
 358 interesting to examine to what extent they are efficient or even whether they are  
 359 optimal. Note that in that scheme, the track has to be segmented to measure  
 360 the track angle on each segment (in  $\approx 19$  cm long segments that contain  $\approx 57$   
 361 hits on average for [39], from which they obtain a relative resolution of 16 % on  
 362 a sample of 4 m tracks with momenta ranging from 0.5 to 4.5 GeV/c). (See also  
 363 [41]).

#### 364 4.1. Single track momentum measurement: Bayesian method

365 Following Matisko and Havlena [24] we obtain <sup>3</sup>, from the measurements,  
 366 the most probable value of  $s$ , and we extract from it an optimal estimator  $\hat{p}$  of  
 367  $p$ . For an event  $A$ , defining  $p_n(A) \equiv p(A|Z^n)$ , we have

$$\begin{aligned}
 p_n(s) &= \frac{p_{n-1}(s, z_n^m)}{p_{n-1}(z_n^m)} \\
 &= \frac{p_{n-1}(s)p_{n-1}(z_n^m|s)}{p_{n-1}(z_n^m)}. \tag{55}
 \end{aligned}$$

We name  $s$ -filter a KF with a gain matrix computed with a given value of  $s$ . We remember (eq. (49)) that the  $s$ -filter innovation probability density function (pdf)  $\beta_n = p_{n-1}(z_n^m|s)$ , is a normal,  $\beta_n = \mathcal{N}(\nu_n(s), 0, S_n(s))$ , where  $\nu_n(s)$  and

---

<sup>3</sup> We assume that the detector spatial resolution  $\sigma$  is known either from calibration on beam or from the analysis of high momentum tracks.

$S_n(s)$  are computed during the filtering process. The  $1/p_{n-1}(z_n^m)$  factor does not vary with  $s$  and is therefore neglected. We obtain

$$p_n(s) \propto \prod_i \beta_i. \quad (56)$$

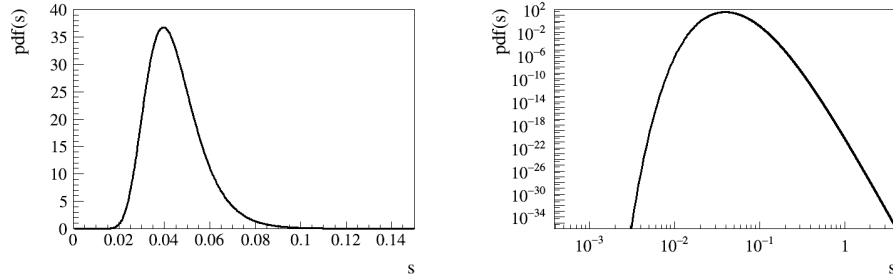


Figure 9:  $p(s)$  distribution for a 50 MeV/c track in a silicon detector (eq. (56)). On that track, the momentum is measured to be equal to 49.9 MeV/c. Linear (left) and logarithmic (right) scales.

The distribution of  $p(s)$  for one simulated 50 MeV/c track is shown in Fig. 9. The track momentum is then obtained from the value of  $s$  that maximizes  $p_n(s)$ :

$$p = p_0 \sqrt{\frac{\Delta x}{lX_0 s}}. \quad (57)$$

368 From the full width half maximum (FWHM) of  $p(s)$  we calculate  $\text{RMS}_s/s$   
 369 and  $\text{RMS}_p/p = (\text{RMS}_s/s)/2$ . The average value of  $\text{RMS}_p/p$  is found to be much  
 370 smaller than the relative RMS  $\sigma_p/p$  of the momentum measurements performed  
 371 on a sample of tracks and shown in Figs. 10 and 11. Our interpretation is that  
 372 the range of  $s$  values compatible within uncertainties with the deflection sample  
 373 of a given track and the fluctuation of the deflection sample from track to track  
 374 are separate quantities. In addition, we observe that the single-track  $p(s)$  width  
 375 and the measured momentum for that track are weakly correlated, so the former  
 376 would add little information to the measurement of the latter.

377 We were not able to obtain an analytical expression for the relative precision  
 378 of the momentum measurement. Instead we performed a parametric variation  
 379 study for a silicon detector with

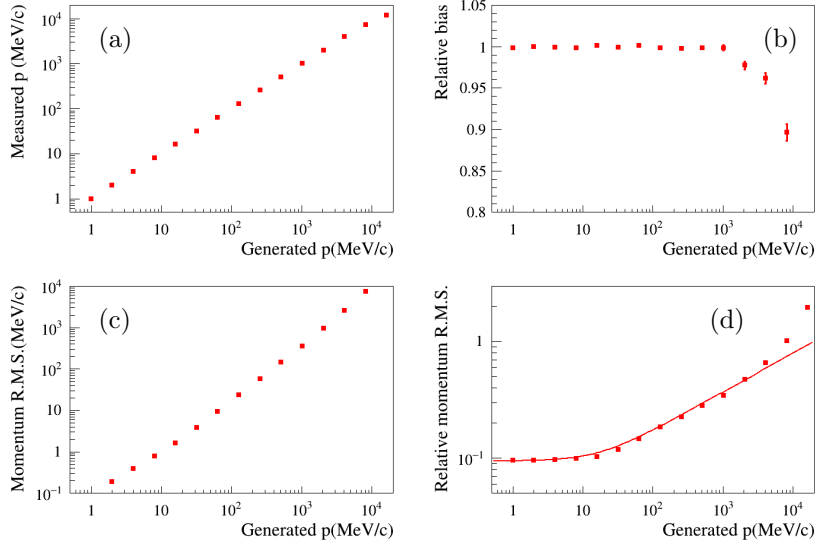


Figure 10: Performance of the momentum measurement for the silicon detector: Variation as a function of the true (generated) particle momentum of (a) the average measured momentum; (b) the average measured normalized to the generated momentum; (c) R.M.S of the measured momenta; (d) the relative R.M.S of the measured momenta. The curve is from eq. (58).

- 380 •  $l = 0.5, 1.0, 2.0$  cm,
- 381 •  $X_0 = 4.685, 9.37, 18.74$  cm,
- 382 •  $N = 23, 46, 56, 92$ ,
- 383 •  $\sigma^2 = 2.5, 5.0, 10.0 \times 10^{-5}$  cm<sup>2</sup>,
- 384 •  $p = 1 \dots 2048$  MeV/c

and with  $\Delta x = 500 \mu\text{m}$ . A good representation of these data is obtained with the following expression:

$$\frac{\sigma_p}{p} \approx \frac{1}{\sqrt{2N}} \sqrt[4]{1 + 256 \left(\frac{p}{p_0}\right)^{4/3} \left(\frac{\sigma^2 X_0}{N \Delta x l^2}\right)^{2/3}}, \quad (58)$$

- from which we obtain the obvious low-momentum asymptote

$$\frac{\sigma_p}{p} \approx \frac{1}{\sqrt{2N}} \quad (59)$$

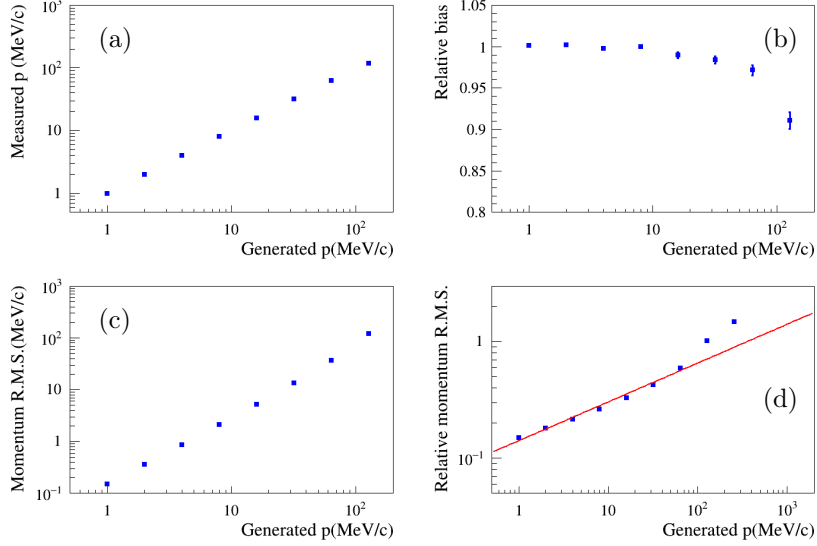


Figure 11: Performance of the momentum measurement for the argon gas detector: Variation as a function of the true (generated) particle momentum of (a) the average measured momentum; (b) the average measured normalized to the generated momentum; (c) R.M.S of the measured momenta; (d) the relative R.M.S of the measured momenta. The curve is from eq. (58).

- and the high-momentum asymptote

$$\frac{\sigma_p}{p} \approx \sqrt{\frac{8}{N}} \left(\frac{p}{p_0}\right)^{1/3} \left(\frac{\sigma^2 X_0}{N \Delta x l^2}\right)^{1/6}. \quad (60)$$

Of particular interest is the momentum,  $p_s$ , above which  $\sigma_p/p$  starts to depart from the low momentum asymptote,

$$p_s = p_0 \frac{1}{64} \left(\frac{N \Delta x l^2}{\sigma^2 X_0}\right)^{1/2}. \quad (61)$$

We define also the momentum,  $p_l$ , above which  $\sigma_p/p$  is larger than unity, which means that the measurement becomes meaningless:

$$p_l = p_0 \left(\frac{N}{8}\right)^{3/2} \left(\frac{N \Delta x l^2}{\sigma^2 X_0}\right)^{1/2}. \quad (62)$$

The only thing that can be said then is that that track is a straight track within uncertainties, that is, with inverse momentum  $1/p$  compatible with zero. These

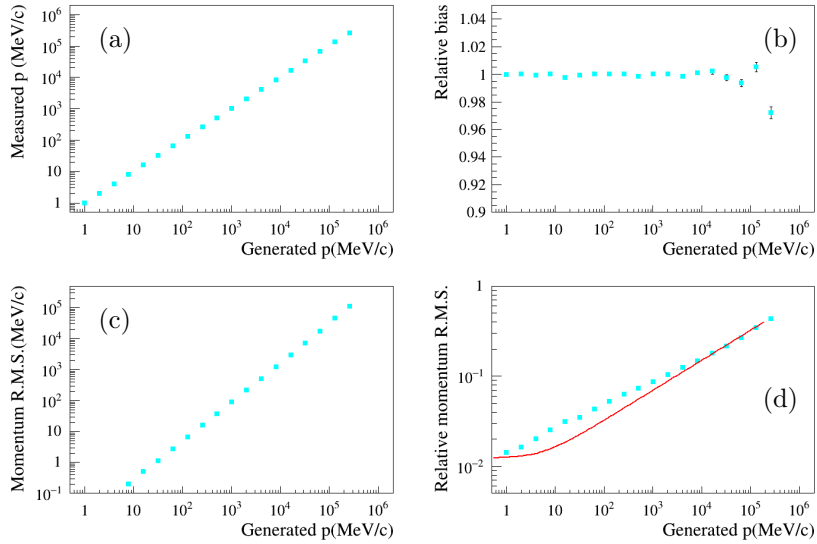


Figure 12: Performance of the momentum measurement for the liquid argon detector: Variation as a function of the true (generated) particle momentum of (a) the average measured momentum; (b) the average measured normalized to the generated momentum; (c) R.M.S. of the measured momenta; (d) the relative R.M.S. of the measured momenta. The curve is from eq. (58). The discrepancy between the data and the curve for this large- $n$  detector, at low momentum that is at very low  $\sigma_p/p$ , needs further investigation.

two momenta are characteristics of the ability to measure track momenta with a given detector and are related to each other,

$$p_\ell = p_s (2N)^{3/2}. \quad (63)$$

Finally, we obtain a simpler expression of the relative momentum resolution,

$$\frac{\sigma_p}{p} \approx \frac{1}{\sqrt{2N}} \sqrt[4]{1 + \left(\frac{p}{p_s}\right)^{4/3}} \quad (64)$$

385 The target relative precision of the DUNE project of 18% is within reach for  
 386 10 m tracks up to a momentum of 17.1 GeV/ $c$  with detector parameter values  
 387 from Table 1 (Fig. 12).

388 *4.2. Comparison with the cell-optimization result*

For the continuous detector,  $\Delta x = l$ , eq. (60) becomes

$$\frac{\sigma_p}{p} = \frac{4}{N^{1/6}\sqrt{2L}} \left(\frac{p}{p_0}\right)^{1/3} (\sigma^2 X_0)^{1/6}, \quad (65)$$

389 that we can compare to the cell-optimization expression (eq. (12) of [11]):

$$\frac{\sigma_p}{p} = \frac{C}{\sqrt{2L}} \left(\frac{p}{p_0}\right)^{1/3} (\sigma^2 X_0)^{1/6} \quad (66)$$

390 with  $C \equiv 5^{1/6} + 5^{-5/6} \approx 1.57$ . We see that the precisions are commensurate  
 391 at small  $N$  and that the present approach becomes more precise at larger  $N$ ,  
 392 within the high-momentum approximation,  $p \gg p_s$ .

393 *4.3. Cramér-Rao Bounds*

The Cramér-Rao bound is a lower bound on the variance of an estimator. If the variance of the estimator reaches the Cramér-Rao bound, it can be stated that the estimate is optimal. The Cramér-Rao criterion for an estimator  $\hat{\theta}$  of a parameter  $\theta$  obtained from measurements  $Z^N$  is [42]:

$$I(\theta) = -\mathbb{E}(\partial_\theta [\partial_\theta p(Z^N|\theta)]), \quad (67)$$

where  $I$  is the Fischer information. If  $\hat{\theta}$  is an unbiased estimator of  $\theta$ , then

$$\mathbb{E}((\hat{\theta} - \theta)^2) \geq I^{-1}(\theta). \quad (68)$$

Following the recursive method of [42] we obtain

$$I(s) = \frac{N}{2s^2}, \quad (69)$$

that is, finally, the obvious

$$\frac{\sigma_p}{p} \geq \frac{1}{\sqrt{2N}}. \quad (70)$$

394 No major insight obtained with the Cramér-Rao Bounds then.

#### 395 4.4. Smoothing and Momentum Measurement

396 In this section 4 we have obtained an optimal estimator of a charged particle  
397 momentum based on the analysis of the filtering innovations of KFs with variable  
398  $s$  parameters. After filtering, a KF provides an optimal estimate of the state  
399 vector parameters (transverse position and angle) of the track at the end of  
400 the track. An optimal estimate all along the track can be obtained by an  
401 additional, backward, pass named smoothing [23]. One might consider a scheme  
402 for momentum measurement based on the smoothing innovations rather than  
403 on the filtering innovations in the hope that the performance would be even  
404 better.

405 Actually smoothing is equivalent to an optimal linear combination of two  
406 independent filterings performed in the direct and in the backward directions,  
407 respectively [43]. We have compared the values of the estimators of the parti-  
408 cle momentum obtained in the two directions and found them to be equal for  
409 each track. Therefore no further improvement is to be expected with such a  
410 combination, nor with a measurement based on smoothing innovations.

## 411 5. Conclusion

412 We first reconsider tracking with multiple scattering and detector resolution  
413 in magnetic-field-free detectors under the assumption that the track momentum  
414 is known, using optimal methods. This is done under a number of approxi-  
415 mations, including Gaussian-distributed multiple-scattering deflections and the  
416 absence of energy loss during propagation. The information matrix is updated  
417 recursively while the track proceeds through the detector: after this mechanism  
418 has converged, the information matrix is found to be a solution of a Riccati  
419 equation which is not surprising as this optimal estimation can be performed  
420 with a Kalman filter.

421 For segmented detectors (discrete Riccati equation) and homogeneous detec-  
422 tors (continuous Riccati equation), we obtain exact expressions of the variances  
423 of the intercept and of the angle from the solution of that equation (eqs. (20)

424 and (37), respectively). We compare their Taylor expansions with expressions  
 425 published in the past. Convergence (**thick detector**) takes place after a detec-  
 426 tor thickness  $L \gtrsim 2.5\lambda$  for homogeneous detectors ( $l \lesssim 0.2\lambda$ ), and for somewhat  
 427 larger values of  $L$  for segmented detectors (Fig. 1).  $\lambda$  is the detector scattering  
 428 length for track momentum  $p$ .

429 For a given track momentum, a **homogeneous detector** is defined as the  
 430 small longitudinal sampling limit,  $l \rightarrow 0$ ,  $i$  and  $s$  being kept constant. In practice  
 431 a limit of  $l/\lambda \lesssim 0.2$  is found (Fig. 4). In contrast with magnetic spectrometers,  
 432 for which the large  $L/\lambda$  Taylor expansion contains  $1/(L/\lambda)^n$  terms, here ( $\vec{B} =$   
 433  $\vec{0}$ ), the expansion contains only exponential terms and convergence is therefore  
 434 much faster (Fig. 7). For coarse segmented detectors for which  $l/\lambda \gtrsim 2$ , e.g.  
 435 for  $p \lesssim 35 \text{ MeV}/c$  for eASTROGAM [8] or AMEGO [7] a KF becomes useless  
 436 as the angular resolution is determined mainly by the measurements in the two  
 437 first wafers (Fig. 3).

438 We then obtain an optimal estimator of the track momentum by a Bayesian  
 439 analysis of the filtering innovations of a series of Kalman filters applied to the  
 440 track. A numerical characterisation of the method shows that for a given de-  
 441 tector the method is reliable up to some limit momentum  $p_\ell$  above which the  
 442 relative precision  $\sigma_p/p$  becomes larger than unity. For lower momentum tracks,  
 443  $p \ll p_\ell$ , the momentum estimation is found to be unbiased. We perform a  
 444 parametric study of the estimator from which we extract a heuristic analyti-  
 445 cal description of the relative uncertainty of the momentum measurement (eq.  
 446 (58)).

## 447 6. Acknowledgment

448 It is a pleasure to acknowledge the support of the French National Research  
 449 Agency (ANR-13-BS05-0002).



450	$\alpha$	one eigenvalue of $\Phi$ with norm larger than 1	eqs. (15), (16)
	$a$	charged particle “intercept” at vertex	eq. (2)
	$b$	charged particle slope at vertex	eq. (2)
	$A_n$	matrix used in the calculation of $I_n$	Subsec. 2.1, see eq. (7)
	$B_n$	matrix used in the calculation of $I_n$	Subsec. 2.1, see eq. (7)
	$B$	scattering matrix	eq. (5)
	$B$	magnetic field	Sec. 1
	$\beta$	charged particle velocity normalized to the velocity of light in vacuum	Sec. 1, see eq. (1)
	$\beta$	scale factor	Subsec. 2.1, see eq. (11)
	$\beta_n$	Kalman innovation probability density	Subsec. 4.1, see eq. (56)
	$\delta$	neutrinos: CP-violating complex phase of the PMNS matrix	Sec. 1
	$D$	drift matrix from layer $n$ to layer $n + 1$	eq. (4)
	$\Delta x$	active target material thickness through which multiple scattering takes place	Sec. 1, see eq. (1)
	$E$	photon energy	Sec. 1
	$\mathbb{E}$	expectation value	Sec. 3
	$\gamma$	charged particle Lorentz factor	Sec. 1
	$H$	Kalman measurement matrix	Sec. 3, see eq. (47)
451	$j$	the imaginary unit	Subsec. 2.1
	$i$	measurement information density per unit track length	Sec. 2, see eq. (6)
	$I$	information matrix	eq. (3) and eq. (67)
	$J$	a constant matrix	eq. (14)
	$K$	Kalman gain matrix	eq. (50)
	$L$	total detector thickness	Sec. 2
	$l$	space between two successive detector layers	Sec. 2, see eq. (4)
	$\lambda$	detector scattering length at momentum $p$	eq. (17)
	$M$	measurement matrix	eq. (6)
	$\nu_n$	Kalman innovations	eq. (48)
	$n$	layer index	Sec. 2
	$N$	number of layers in detector	Sec. 2
	$\mathcal{N}$	normal or Gaussian probability density	eq. (54)
	$\Phi$	matrix that performs the transformation from $\begin{bmatrix} A_n \\ B_n \end{bmatrix}$ to $\begin{bmatrix} A_{n+1} \\ B_{n+1} \end{bmatrix}$	eq. (9)
	$p$	probability density	Sec. 3, see eq. (53)
	$p$	charged particle momentum	Sec. 1
	$p_0$	multiple scattering constant	Sec. 1, see eq. (1)

452

$p_1$	detector tracking angle resolution characteristic momentum	eq. (38)
$p_u$	detector thin/thick limit momentum	eq. (40)
$p_x$	detector homogeneous/segmented limit momentum	eq. (42)
$p_s$	detector limit momentum between the $\sigma_p/p = 1/\sqrt{2N}$ and $\sigma_p/p \propto p^{1/3}$ ranges	eq. (61)
$p_\ell$	detector limit momentum for which $\sigma_p/p = 1$	eq. (62)
$P_n$	Kalman state covariance matrix	Sec. 3, see eq. (46)
$q$	particle electric charge	Sec. 1
$\rho$	charged particle trajectory curvature radius	Sec. 1
$\sigma$	single-track single-layer space resolution	Sec. 1
$\sigma_p$	momentum resolution	Sec. 1
$s$	average multiple scattering angle variance per unit track length	Sec. 2, see eq. (5)
$S_n$	Kalman innovation covariance matrix	eq. (49)
$\theta$	a parameter	Sec. 4.3, see eq. (67)
$\hat{\theta}$	estimator for parameter $\theta$	Sec. 4.3, see eq. (67)
$\theta_0$	multiple scattering RMS angle	eq. (1)
453 $u$	detector thickness normalized to detector scattering length at momentum $p$	eq. (18)
$u_n$	deflection angle	Sec. 3, see eq. (44)
$v_n$	Kalman measurement noise	Sec. 3, see eq. (47)
$V$	particle state vector (“intercept”, angle) correlation matrix	Sec. 2, see eq. (3)
$X_0$	active target material radiation length	Sec. 1, see eq. (1)
$x$	detector longitudinal sampling normalized to scattering length at momentum $p$	Subsec. 2.1, see eq. (16)
$x$	axis name	
$x_n$	Kalman state vector	eq. (44)
$X$	matrix used in the calculation of $\Phi'$	eq. (34)
$Y$	matrix used in the calculation of $\Phi'$	eq. (34)
$y$	axis name	
$z_n$	Kalman measurements	eq. (47)
$z$	axis name	
$Z$	active target atomic number	Sec. 1
$Z_n$	set of measurements, $z_0 \cdots z_n$	Sec. 3, see eq. (53)

454 **References**

- 455 [1] T. Tanimori *et al.*, “Establishment of Imaging Spectroscopy of Nuclear Gamma-Rays  
456 based on Geometrical Optics,” *Sci. Rep.* **7** (2017) 41511, [arXiv:1702.01483 [physics.ins-  
457 det]].
- 458 [2] T. J. O’Neill *et al.*, “The TIGRE gamma-ray telescope”, *AIP Conf. Proc.* **587** (2001)  
459 882.
- 460 [3] G. Kanbach *et al.*, “Development and calibration of the tracking Compton/Pair telescope  
461 MEGA”, *Nucl. Instrum. Meth. A* **541** (2005) 310.
- 462 [4] F. Lebrun *et al.*, “CAPSiTT: Compton Large Area Silicon Timing Tracker for Cosmic  
463 Vision M3”, *PoS(INTEGRAL 2010)* 034.
- 464 [5] A. Morselli *et al.*, “GAMMA-LIGHT: High-Energy Astrophysics above 10 MeV,” *Nuclear*  
465 *Physics B Proc. Supp.* **239-240** (2013) 193.
- 466 [6] A. A. Moiseev *et al.*, “Compton-Pair Production Space Telescope (ComPair) for MeV  
467 Gamma-ray Astronomy,” arXiv:1508.07349 [astro-ph.IM].
- 468 [7] J. McEnergy *et al.*, “Allsky Medium Energy GammaRay Observatory (AMEGO)”, Sub-  
469 mitted to the Physics of the Cosmos Program Analysis Group Call for White Papers:  
470 Probe-Class Astrophysics Mission Concepts, March 2016.
- 471 [8] A. De Angelis, V. Tatischeff *et al.*, “The e-ASTROGAM mission: Exploring the extreme  
472 Universe with gamma rays in the MeV – GeV range”, [arXiv:1611.02232], to appear in  
473 *Exp Astron* (2017), doi:10.1007/s10686-017-9533-6.
- 474 [9] X. Wu *et al.*, “PANGU: A High Resolution Gamma-ray Space Telescope,” **SPIE2014**  
475 (2014) 91440F, [arXiv:1407.0710 [astro-ph.IM]].
- 476 [10] S. Takahashi *et al.*, “GRAINE project: The first balloon-borne, emulsion gamma-ray  
477 telescope experiment,” *PTEP* **2015** (2015) 043H01.
- 478 [11] D. Bernard, “TPC in gamma-ray astronomy above pair-creation threshold,” *Nucl. In-*  
479 *strum. Meth. A* **701**, 225 (2013) Erratum: [*Nucl. Instrum. Meth. A* **713**, 76 (2013)].  
480 [arXiv:1211.1534 [astro-ph.IM]].
- 481 [12] D. Bernard, “Polarimetry of cosmic gamma-ray sources above  $e^+e^-$  pair creation thresh-  
482 old”, *Nucl. Instrum. Meth. A* **729** (2013) 765. [arXiv:1307.3892 [astro-ph.IM]].
- 483 [13] P. Gros *et al.*, “Measurement of polarisation asymmetry for gamma rays between 1.7 to  
484 74 MeV with the HARPO TPC”, **SPIE2016**, 9905-95, arXiv:1606.09417 [astro-ph.IM].

- 485 [14] P. Gros and D. Bernard, “ $\gamma$ -ray polarimetry with conversions to  $e^+e^-$  pairs: polarization  
486 asymmetry and the way to measure it,” *Astropart. Phys.* **88** (2017) 30, [arXiv:1611.05179  
487 [astro-ph.IM]].
- 488 [15] D. Bernard, on behalf of the HARPO Collaboration, “HARPO: 1.7 - 74 MeV gamma-  
489 ray beam validation of a high angular resolution, high linear polarisation dilution, gas  
490 time projection chamber telescope and polarimeter,” presented at SciNeGHE 2016, Pisa,  
491 Italy. Proceedings arXiv:1702.08429 [astro-ph.IM], to appear in *Il Nuovo Cimento* 40 C  
492 (2017).
- 493 [16] S. P. Wakely *et al.*, “Transition radiation detectors for energy measurements at high  
494 Lorentz factors,” *Nucl. Instrum. Meth. A* **531** (2004) 435.
- 495 [17] R. Acciarri *et al.* [DUNE Collaboration], “Long-Baseline Neutrino Facility (LBNF) and  
496 Deep Underground Neutrino Experiment (DUNE) : Volume 2: The Physics Program for  
497 DUNE at LBNF,” arXiv:1512.06148 [physics.ins-det].
- 498 [18] R. Acciarri *et al.* [DUNE Collaboration], “Long-Baseline Neutrino Facility (LBNF) and  
499 Deep Underground Neutrino Experiment (DUNE) : Volume 4 The DUNE Detectors at  
500 LBNF,” arXiv:1601.02984 [physics.ins-det].
- 501 [19] A. Ankowski *et al.* [ICARUS Collaboration], “Measurement of through-going particle  
502 momentum by means of multiple scattering with the ICARUS T600 TPC,” *Eur. Phys.*  
503 *J. C* **48** (2006) 667
- 504 [20] G. Molière, “Theorie der Streuung schneller geladener Teilchen. III. Die Vielfachstreuung  
505 von Bahnspuren unter Berücksichtigung der statistischen Kopplung”, *Zeitschrift Natur-*  
506 *forschung A* **10** (1955) 177.
- 507 [21] K. Kodama *et al.*, “Momentum measurement of secondary particle by multiple Coulomb  
508 scattering with emulsion cloud chamber in DONuT experiment,” *Nucl. Instrum. Meth.*  
509 *A* **574** (2007) 192.
- 510 [22] N. Agafonova *et al.* [OPERA Collaboration], “Momentum measurement by the Multiple  
511 Coulomb Scattering method in the OPERA lead emulsion target,” *New J. Phys.* **14**  
512 (2012) 013026 [arXiv:1106.6211 [physics.ins-det]].
- 513 [23] R. Frühwirth, “Application of Kalman filtering to track and vertex fitting,” *Nucl. In-*  
514 *strum. Meth. A* **262** (1987) 444.
- 515 [24] P. Matisko and V. Havlena, “Noise covariance estimation for Kalman filter tuning using  
516 Bayesian approach and Monte Carlo”, *Int. J. Adapt. Control Signal Process.* **27** (2013)  
517 957.

- 518 [25] X. Wu, "PANGU: A High Resolution Gamma-Ray Space Telescope," PoS **ICRC2015**  
519 (2016) 964.
- 520 [26] C. Patrignani *et al.* [Particle Data Group], "Review of Particle Physics," Chin. Phys. C  
521 **40** (2016) 100001.
- 522 [27] P. Billoir, "Track Fitting With Multiple Scattering: A New Method," Nucl. Instrum.  
523 Meth. A **225** (1984) 352.
- 524 [28] W. R. Innes, "Some formulas for estimating tracking errors," Nucl. Instrum. Meth. A  
525 **329** (1993) 238.
- 526 [29] S. Grewal and P. Andrews, "Kalman Filtering, theory and practice using Matlab", 2nd  
527 edition, Wiley Interscience publication, (2001)
- 528 [30] M. Adam and N. Assimakis, "Nonrecursive solution for the discrete algebraic Riccati  
529 equation and  $X + A * X - 1A = L$ ", Open Mathematics **13.1** (2015) 51-63.
- 530 [31] Wolfram Mathematica
- 531 [32] P. Yuantong "Hamiltonian Matrices and the Algebraic Riccati Equation", Technische  
532 Universität Chemnitz, 2009.
- 533 [33] K. Fujii, "Extended Kalman Filter" The ACFA-Sim-J Group
- 534 [34] R. K. Mehra, "On the identification of variances and adaptive Kalman filtering", IEEE  
535 Trans. Automat. Control **15** (1970) 175-184.
- 536 [35] Mehra, R., "Approaches to adaptive filtering", IEEE Trans. Automat. Control **17** (1972)  
537 903-908.
- 538 [36] B. J. Odelson, M. R. Rajamani, J. B. Rawlings, "A new autocovariance least-squares  
539 method for estimating noise covariances", Automatica **42** (2006) 303-308.
- 540 [37] P. R. Belanger, "Estimation of noise covariance matrices for a linear time varying stochas-  
541 tic process", Automatica **10** (1974) 267-275.
- 542 [38] L. Stanco, "Particle track reconstruction in heavy materials with the Kalman technique,"  
543 Comput. Phys. Commun. **57** (1989) 380.
- 544 [39] M. Antonello *et al.*, "Muon momentum measurement in ICARUS-T600 LAr-TPC via  
545 multiple scattering in few-GeV range," arXiv:1612.07715 [physics.ins-det].
- 546 [40] J. Duník, M. Šimandl, O. Straka, "Methods for Estimating State and Measurement Noise  
547 Covariance Matrices: Aspects and Comparison", IFAC Proceedings Volumes **42** (2009)  
548 372-377.

- 549 [41] P. Abratenko *et al.* [MicroBooNE Collaboration], "Determination of muon momentum  
550 in the MicroBooNE LArTPC using an improved model of multiple Coulomb scattering,"  
551 arXiv:1703.06187 [physics.ins-det].
- 552 [42] P. Matisko, V. Havlena, "Cramér-Rao Bounds for Estimation of Linear System Noise  
553 Covariances", *Journal of Mechanical Engineering and Automation* **2** (2012) 6-11.
- 554 [43] D. C. Fraser, "A New Technique for the Optimal Smoothing of Data", Sc.D. Dissertation,  
555 Mass. Inst. Tech., Cambridge, MA, 1967.

556	<b>Contents</b>	
557	<b>1 Introduction</b>	<b>1</b>
558	1.1 $\gamma$ -ray astronomy . . . . .	1
559	1.2 Large noble-liquid TPCs for neutrino physics . . . . .	3
560	1.3 Track momentum measurement from multiple scattering . . . . .	4
561	<b>2 Tracking</b>	<b>7</b>
562	2.1 Segmented detector . . . . .	8
563	2.1.1 Segmented detector: Thick detector limit . . . . .	10
564	2.2 Homogeneous Detector . . . . .	13
565	2.2.1 Homogeneous thick detector: Exact solution . . . . .	15
566	2.2.2 Variation of the angle variance along the track . . . . .	16
567	2.3 Optimal tracking: wrap up . . . . .	17
568	<b>3 Kalman filter</b>	<b>21</b>
569	<b>4 Momentum Measurement</b>	<b>23</b>
570	4.1 Single track momentum measurement: Bayesian method . . . . .	25
571	4.2 Comparison with the cell-optimization result . . . . .	30
572	4.3 Cramér-Rao Bounds . . . . .	30
573	4.4 Smoothing and Momentum Measurement . . . . .	31
574	<b>5 Conclusion</b>	<b>31</b>
575	<b>6 Acknowledgment</b>	<b>32</b>